Substituent Effect on Vibrationally Resolved Absorption Spectra and Exciton Dynamics of Dipyrrolonaphthyridinedion Aggregates

Shishi Feng, Yi Zhao,* and WanZhen Liang*

State Key Laboratory of Physical Chemistry of Solid Surfaces, iChEM, Fujian Provincial Key Laboratory of Theoretical and Computational Chemistry, and College of Chemistry and Chemical Engineering, Xiamen University, Xiamen 361005, People's Republic of China

E-mail: yizhao@xmu.edu.cn; liangwz@xmu.edu.cn

*To whom correspondence should be addressed

Abstract

Dipyrrolonaphthyridinedion (DPND) thin films exhibit interesting photo-physical properties and singlet fission (SF) processes. A recent experimental work found that the alkyl substitution in DPND skeleton has the remarkable influence on the characteristics of electronic absorption spectra and SF rates. Here, we theoretically elucidate the microscopic mechanism of the substituent effect on the optical properties and exciton dynamics of materials by combining the electronic structure calculations and the quantum dynamics simulations. The results show that the alkyl substituent has a minor effect on the single molecular properties, but dramatically changes these of DPND aggregates via varying the intermolecular interactions. The aggregates of DPND with and without alkyl side chains exhibit the more-likely of characters of H-type aggregations. In the former (DPND6), the weak degree of mixing of intramolecular localized excited (LE) states and intermolecular charge transfer (CT) states makes the low-energy absorption band possess the predominant optical absorption, while in the latter (DPND), the CT and LE states are close in energy, together with their strong interaction, resulting in the substantial state-mixing, so that its two low-energy absorption bands have nearly equal oscillator strengths and a wide energy spacing of more than 0.5 eV. The simulation of exciton dynamics elucidates that the photo-initiated states in both aggregates cannot generate the free charge carrier because of the lack of enough driving forces. However, the population exchanges between LE and CT states in DPND aggregates are much faster than in DPND6 aggregates, indicating the different SF behaviors, consistent with the experimental observation.

Introduction

It is well-known that photo-induced energy transfer and charge transfer (CT) are one of key factors for determining the device performances in the light harvesting systems and organic photovoltaics.[1–4] These photophysical properties are closely related to the molecular microstructures and stacking arrangements, and finding the structure-property relationship thus becomes extremely important. Experimentally, a variaty of techniques have been proposed

to regulate the intermolecular packing arrangement to improve the device efficiency, such as modulating the substitution positions, increasing the lengths of chains or directly adopting the high-pressure technique.[5–10] To microscopically reveal the underlying correlations between properties and stacking structures, one further requires electronic structure calculations and photo-induced carrier dynamic simulations.

Dipyrrolonaphthyridinedion (DPND) has a series of cross-conjugated skeletons composed of electron-rich pyrrole rings and electron-poor carbonyl moieties, and is a kind of effective singlet fission materials with exceptional photophysical properties[11–13] such as suitable energy level, good stability, high fission efficiency and adjusting molecular structures. The two DPND molecules, one with (DPND6) and the other without (DPND) alkyl side chains, exhibit the quite different photophysical properties in thin films, especially in the spectral characteristics and dynamics processes.[12,14] For instance, the DPND thin film with the H-type aggregation has an accelerated singlet fission process compared to the DPND6 thin film, and the faster singlet fission process in DPND is attributed to the formation of a CT/excimer mixed state, in which the CT state is close in energy with Frenkel exciton (FE) and excimer states, which could drive excited-state population escaping from excimer trap and promote an ultrafast and highly efficient singlet fission process. The mechanism of CT state-mediated singlet fission has also been used by many others to explain their experimental measurements.[15–19]

Essentially, the FE-CT mixed states can remarkably affect electronic absorption spectra.[20] In our previous work,[21–23] we have clearly demonstrated that the mixing between a bright FE state and a dark CT state can lead to the two absorption peaks, and the relative peak intensities are closely associated with the intermolecular distances, aggregation lengths and long-range excitation energy transfer. Indeed, the experiments[14] have shown that the DPND thin film has an obviously enhanced absorption band in the region of 300-450 nm, quite different from DPND6, and their absorption spectra around 500-600 nm also exhibit different properties. Although those spectral differences come from the different mixing components of FE/CT states,[12] it is still absent of the detailed spectral assignments. This paper aims to theoretically establish the detailed relationship

of spectra and aggregate stacking arrangement to confirm this assignment.

The experimental synthesis shows that the substituent of alkyl side chain can significantly change crystal structures of DPND. For instance, the DPND6 and DPND aggregates have different transverse and longitudinal shifts and intermolecular distances. Those structure differences result in quite different mixing components of FE and CT states in the adiabatic excited states, subsequently produce the different absorption spectral characters. However, it is nontrivial to reveal the structure-property relationship in organic aggregates because of complex dynamic processes from many-body interactions,[24–28] such as the long-range excitation energy transfer, electron and hole transfer and molecular vibrational motions, etc.

Focusing on photo-physical processes in organic aggregates, our group has developed the approaches for constructing the effective model Hamiltonian for describing the aggregates[29] and simulating the coupled exciton-vibrational dynamics.[30] The fragment particle and hole densities (FPHD) method[29] has been proposed to obtain the energies and electronic couplings among quasi-diabatic states from the properties of adiabatic excited states. Based on the model Hamiltonian, non-Markovian stochastic Schrödinger equations[30] have been developed to describe photo-physical processes for the systems with multiple electronic states. These approaches can be straightforwardly adopted to calculate vibrationally-resolved absorption spectra for complex systems. Indeed, we used those approaches to investigate the absorption spectra in Zinc Phthalocyanine aggregates.[21–23]

With available approaches, we theoretically investigate the vibrationally resolved absorption spectra and exciton dynamics processes of two kinds of DPND aggregates here. In the work, we discuss in detail the influence of the alkyl side chain in electronic-state properties and explain the origin of different spectral characteristics for two DPND aggregates. Furthermore, we also show the dynamics behaviors of two DPND thin films in the low-energy and high-energy region. The paper is arranged as follows: Sec. II outlines the theoretical methods and presents calculations details, Sec. III is the results and discussion and Sec. IV is the conclusions.

Methods

Model Hamiltonian

For a N-monomer aggregate, the total Hamiltonian consists of the electronic, vibrational and electron-phonon interaction terms

$$\hat{H}_{\text{agg}} = \hat{H}_{el} + \hat{H}_{ph} + \hat{H}_{el-ph}. \tag{1}$$

Here, the electronic Hamiltonian $\hat{H}_{el}$ includes the localized excited (LE), CT and charge-separated (CS) states, and it can be expressed as follows

$$\begin{aligned} \hat{H}_{el} = & \sum_{nmi} E_{n,m;L_i} |n,m;L_i\rangle\langle n,m;L_i| \\ & + \sum_{nmi} \sum_{n'm'i'}{}' V_{nm,n'm';L_iL_{i'}} |n,m;L_i\rangle\langle n',m';L_{i'}|. \end{aligned} \tag{2}$$

Here, $|n,m;L_i\rangle$ represents the electronic excited state. For $n \neq m$, it represents that the n-th monomer is in the cationic state and the m-th monomer is in the anionic state, for $n = m$, it corresponds to a LE state with the n-th monomer excited, and all other monomers are in the ground state. L_i orders the electronic states for a given $|n,m\rangle$ state. $E_{n,m;L_i}$ is the vertical excitation energy of state $|n,m;L_i\rangle$ and $V_{nm,n'm';L_iL_{i'}}$ corresponds to the electronic coupling between state $|n,m;L_i\rangle$ and $|n',m';L_{i'}\rangle$. Under this notation representation, the electronic Hamiltonian includes the LE states when $n = m$, bounded CT states when $|n-m| = 1$ and CS states when $|n-m| \geq 2$. As a result, $L_i * N^2$ electronic states are incorporated in the electronic Hamiltonian.

The vibrational Hamiltonian can be described as

$$\hat{H}_{ph} = \sum_n \sum_j \omega_j \left(\hat{b}_{nj}^{\dagger} \hat{b}_{nj} + \frac{1}{2} \right), \tag{3}$$

where $\hat{b}_{nj}^{\dagger}$ and $\hat{b}_{nj}$ represent the creation and annihilation operator of the j-th vibrational mode in the n-th monomer with the frequency of ω_j, respectively.

The electron-phonon interaction term is given by

$$\hat{H}_{e-ph} = \sum_{n}\sum_{j} \omega_j (\hat{b}^{\dagger}_{nj} + \hat{b}_{nj}) \otimes \hat{x}_{nj} \tag{4}$$

with

$$\begin{aligned} \hat{x}_{nj} = & \sum_{i} g^{ex}_{j,L_i} |n,n;L_i\rangle\langle n,n;L_i| + \sum_{i}\sum_{m\neq n} g^{+}_{j} |n,m;L_i\rangle\langle n,m;L_i| \\ & + \sum_{i}\sum_{m\neq n} g^{-}_{j} |m,n;L_i\rangle\langle m,n;L_i|, \end{aligned} \tag{5}$$

where $\hat{x}_{nj}$ corresponds to the electron-phonon interaction operator coupled with the different electronic states. g^{ex}_{j,L_i}, g^{+}_{j}, and g^{-}_{j} are the electron-phonon coupling constant of the j-th vibrational mode associated with the i-th excited, cationic and anionic state of the monomer, respectively.

There are several numerical techniques for the calculations of electron-phonon interactions.[31–33] Here, we adopt the vertical gradient (VG) approximation,[34–36] in which g_j factor is calculated by

$$g_j = \sqrt{\frac{1}{2\omega_j^3}} \frac{dV}{dQ_j}, \tag{6}$$

where V and Q_j are the potential energy of corresponding electronic excited states and the coordinate of the j-th normal mode, respectively. The VG approximation assumes that the excited-state potential energy surface (PES) is just a shifted PES of the ground state, meaning that the electronic excitation does not significantly change the shape of the PES. For DPND molecules, the VG approximation should be suitable due to their planar and rigid structures according to our previous experience.[23]

In the absorption spectral calculation, we need to know the transition dipole operator, which is given by

$$\hat{\boldsymbol{\mu}} = \sum_{nmi} \vec{\mu}_{n,m;L_i} \left(|n,m;L_i\rangle\langle g| + |g\rangle\langle n,m;L_i| \right), \tag{7}$$

where $\vec{\mu}_{n,m;L_i}$ represents the transition dipole moment vector between the ground state $|g\rangle$ and electronic state $|n,m;L_i\rangle$.

Parametrization of Electronic Hamiltonian

To parameterize the electronic Hamiltonian of Eq. (2), we adopt the FPHD method[29] to obtain the corresponding Hamiltonian parameters including the transition dipole moments, states energies and couplings between the various different states in the quasi-diabatic representation. The central idea of FPHD is to search for orthonormal electronic states that maximally localize electron and hole densities in terms of predefined molecular fragments.

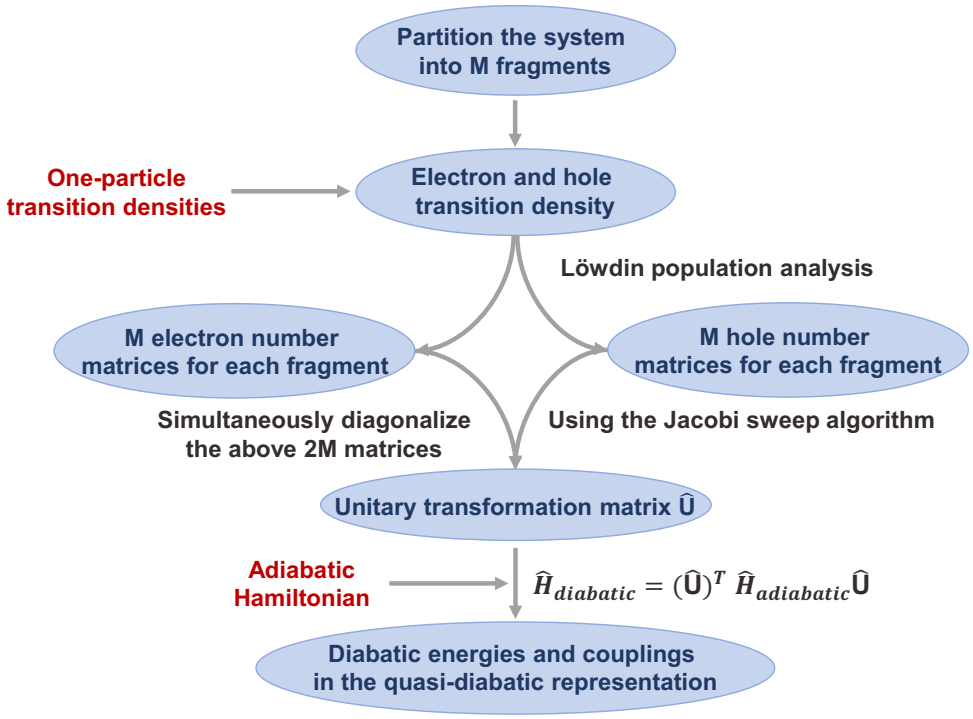

Figure 1: Schematic diagram of the implementation process of FPHD method.

Fig. 1 shows the implementation process of FPHD method. Firstly, the molecular fragments are partitioned based on the investigated molecular aggregates. The transition density matrices in the adiabatic representation are used to calculate electron and hole number matrices of predefined fragments. Then, the unitary transformation matrix is obtained by simultaneously diagonalizing

the number matrices using the Jacobi sweep algorithm. Finally, the corresponding parameters in the quasi-diabatic representation such as transition dipole moments, energies and couplings are obtained by the adiabatic-to-diabatic transformation based on the obtained unitary transformation matrix.

Calculation of Vibrationally-resolved Electronic Absorption Spectra

Once the model Hamiltonian is known, the dynamics processes and absorption spectra can be simulated using non-Markovian stochastic Schrödinger equation (NMSSE),[38,39] which is written as

$$i\frac{\partial}{\partial t}|\psi_\xi(t)\rangle = \Bigg[\hat{H}_{el} + \sum_{nj}\xi_{nj}(t)\hat{x}_{nj} - i\sum_{nj}\hat{x}_{nj}\int_0^t \hat{x}_{nj}(-\tau)\alpha_j^{res}(\tau)\mathrm{d}\tau\Bigg]|\psi_\xi(t)\rangle, \tag{8}$$

where $|\psi_\xi(t)\rangle$ is the time-dependent stochastic wavefunction and $\xi_{nj}(t)$ is the phonon-induced stochastic field. $\hat{x}_{nj}(t) \equiv e^{i\hat{H}_{el}t}\hat{x}_{nj}e^{-i\hat{H}_{el}t}$. Here, the residual correlation function is expressed as

$$\alpha_j^{res}(t) = \tanh\frac{\beta\omega_j}{4}\cos\omega_j t - i\sin\omega_j t. \tag{9}$$

In the dynamics simulations, the molecular vibrations are in the ground state at thermal equilibrium initially.

In order to obtain the vibrationally resolved absorption spectra of aggregates, we adopt the linear response theory to obtain the line shape function of spectra via Fourier transforming the correlation function.

$$D(\omega) = \frac{1}{2\pi}\Re\int_0^\infty C_{\mu\mu}(t)e^{i\omega t}\mathrm{d}t, \tag{10}$$

where $\Re$ represents to take the real part and the correlation function is given by

$$C_{\mu\mu}(t) = \mathrm{Tr}\left\{ e^{i\hat{H}_{agg}t}\hat{\boldsymbol{\mu}}e^{-i\hat{H}_{agg}t}\cdot\hat{\boldsymbol{\mu}}|g\rangle\langle g|\frac{e^{-\beta\hat{H}_{ph}}}{Z_{ph}}\right\} \tag{11}$$

where $|g\rangle$ is the ground state of aggregates and $Z_{ph} \equiv \mathrm{Tr}\{e^{-\beta\hat{H}_{ph}}\}$ is the phonon partition function. In the framework of NMSSE, the correlation function can be described as

$$C_{\mu\mu}(t) = M\left[\langle g|\hat{\mu}|\psi_\xi(t)\rangle\right]_\xi, \tag{12}$$

where $M[\cdot]_\xi$ represents to take the average for the stochastic fields, and the initial condition is given by

$$|\psi_\xi(0)\rangle = \hat{\mu}|g\rangle. \tag{13}$$

Concretely speaking, we start from Eq. (13), and solve Eq. (8) to obtain $|\psi_\xi(t)\rangle$. We then calculate the correlation function using Eq. (12) and obtain the line shape function of spectra by Fourier transform of the correlation function. Finally, the corresponding absorption spectra of aggregates can be obtained by multiplying the lineshape functions with the absorption frequency. More detailed implementation for the calculations of the exciton dynamics processes and vibrationally resolved absorption spectra in an aggregate using Eq. (8) can refer to Ref. 21, 22 and 23.

Quantum Chemical Calculations

The initial structures of DPND6 and DPND monomers are extracted from the crystal structures [12,14] and then they are optimized by using the density functional theory (DFT) with the exchange-correlation (XC) functional B3LYP. The basis set of def2-TZVP is adopted and the Grimme3 dispersion correction to DFT is included. The vertical excitation energies and the corresponding oscillator strengths are calculated by time-dependent DFT (TD-DFT) with the tuned long-range-corrected XC functional LC-ωPBE with $\omega = 0.157$ for DPND6 and $\omega = 0.193$ for DPND and the basis set of 6-311G(d,p). The vibrational frequency analysis for the ground state of DPND6 and

DPND monomer either in DCM solution or in crystal environment are carried out at the level of B3LYP/def2-TZVP and all the vibrational frequencies are scaled by a scaling factor of 0.959[40] accounting for the anharmonicity effect. All the vibrational modes (a total of 180 for DPND6 and 72 for DPND monomer) are involved in the simulations. All the calculations are carried out within Gaussian 16 program package.[41] The solvent and crystal environment are incorporated by using the solvent model of density (SMD)[42] and the dielectric constants for DPND6 and DPND crystals are set to be 4.6 and 3.4, respectively.[14]

To construct the electronic Hamiltonian of aggregates, we carry out the diabatization processes of DPND6 and DPND hexamers. The total number of 180 low-lying adiabatic states are included. After the diabatization, 180 quasi-diabatic states with different charge and excitation distributions are generated. However, because the low-energy quasi-diabatic states play the major role on the spectral characters and dynamics processes, we only involve two lowest-lying quasi-diabatic states for each charge and excitation distribution in the calculations. The corresponding Hamiltonian parameters for the N-monomer aggregate are provided in the supporting information based on the hexamer results.

The electron-phonon interaction constants associated with the localized excited, cationic and anionic states can be obtained based on the DPND6 and DPND single monomer in the crystal environment and the corresponding results have been showed in the supporting information. In addition, the spectral and dynamics simulations in the DPND6 and DPND aggregates are implemented at 300 K based on above-mentioned Hamiltonian parameters. The electron and hole distributions are exported and visualized with Multiwfn 3.8[43] and VMD 1.9.3[44] software.

Results and Discussion

Absorption and Emission Spectra of DPND6 and DPND Monomers

The DPND6 monomer has the same cross-conjugate skeleton as the DPND monomer except it has the alkyl side chains. The molecular geometries of DPND6 and DPND are inserted in Fig.2.

To investigate whether the substituent itself joins the molecular photo-physical processes, we first calculate the electronic absorption and emission spectra of DPND6 and DPND monomers with the inclusion of vibration motions. The calculated results are shown in Fig. 2, in which

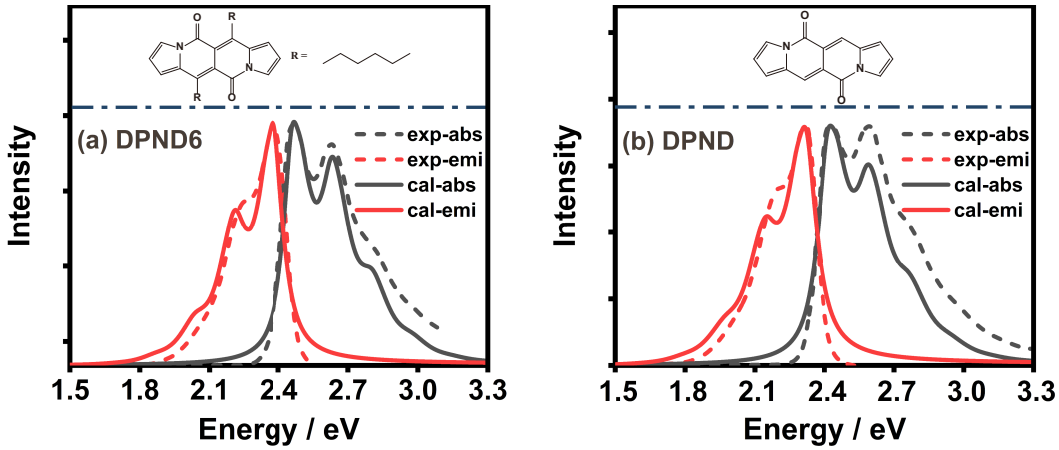

Figure 2: Vibrationally resolved absorption and emission spectra of DPND6 (a) and DPND (b) monomer in dichloromethane solvent. The black and red line correspond to the absorption and emission spectra, respectively. The calculated spectra of DPND6 and DPND are blue-shifted by 0.090 eV and 0.080 eV, respectively. The dashed lines represent the experimental results[12,14] for comparison. The chemical structures of DPND6 and DPND molecules are shown and the hydrogen atoms have been omitted for simplification.

we have included the outer reorganization energies of 0.038 eV and 0.045 eV for DPND6 and DPND to fit the observed Stokes shifts. It is seen that both monomers have very similar spectral shapes, and the vibrationally-resolved peaks are mainly from the stretching vibration of cross-conjugated skeletons with frequencies of 1356 cm^{-1} and 1360 cm^{-1} for DPND6 and DPND monomers, respectively. These data manifest that the alkyl side chain has a slight perturbation to electronic excited states, and the molecular excited-state properties as well as photo-physical processes should be dominantly determined by the cross-conjugate skeletons. Therefore, in the later calculations the hexyl side chain is replaced by the ethyl side chain to save computation costs. It is also noted that our theoretical calculation with the VG approximation reasonably produces the experimental absorption and emission spectral lineshapes regardless the slight difference in peaks' relative intensities.

DPND6 and DPND Aggregates

Although the alkyl side chain itself does not directly contribute to the spectra of monomers, it has a significant effect on stacking arrangements of aggregates. Fig. 3 displays the crystal structures of DPND6[12] and DPND[14] from the experimental measurements, where the relative displacements of corresponding dimer are presented. In both crystals, these normal one-dimensional direction with respect to the horizontal direction dominates the spectra and dynamics processes because the interactions between two columns are much weaker than those between monomers along this direction. In dynamic simulations, we thus only consider the one-dimensional molecular chain. Along this molecular chain, the relative transverse and longitudinal shift are 3.02 and 1.32 Å in

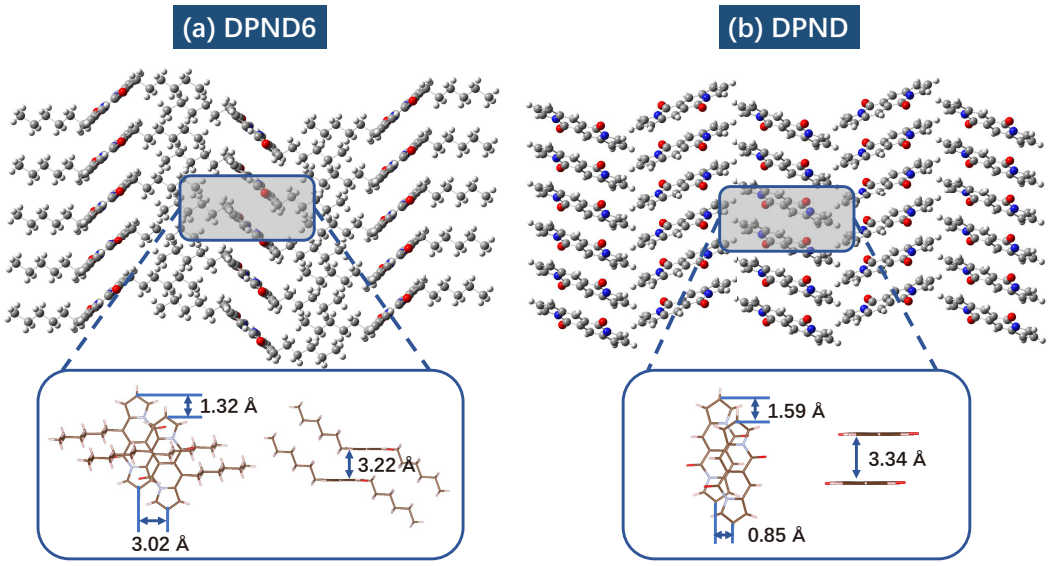

Figure 3: Crystal structures of (a) DPND6 and (b) DPND aggregates. The two magnification boxes represent the relative transverse, longitudinal and vertical offset in DPND6 and DPND dimer extracted from the corresponding crystal structures, respectively.

the DPND6 crystal, whereas they become 0.85 and 1.59 Å in the DPND crystal. Moreover, the intermolecular distances between two monomers are also different and they are 3.22 and 3.34 Å in DPND6 and DPND crystals, respectively. These obvious stacking discrepancies may lead to different spectral characteristics and dynamics processes.

Diabatization of DPND6 and DPND Hexamer

Based on vertical adiabatic electronic excitation properties of aggregates, the FPHD method can produce the energies of quasi-diabatic states and electronic couplings among them. The major diabatization results of the DPND6 and DPND hexamer in the low-energy regime are presented in Fig. 4 and Fig. 5, and more numerical results can be found in the supporting information. Herein, the hexyl side chain in DPND6 is substituted by the ethyl side chain for the calculation of adiabatic electronic states in order to save calculations costs.

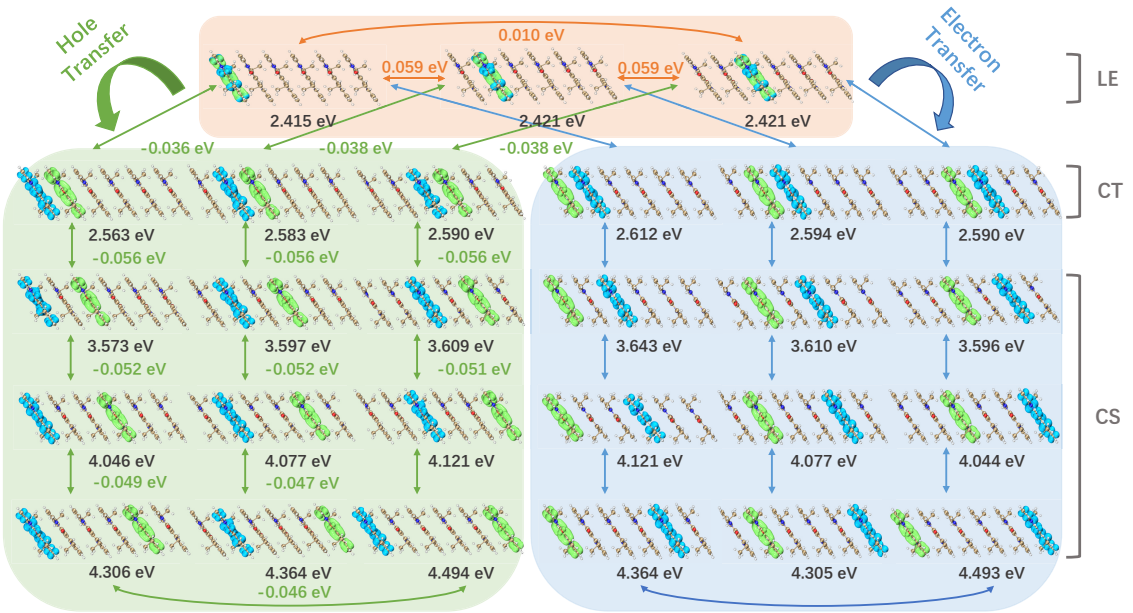

Figure 4: The energies of quasi-diabatic LE, CT and CS states and electronic couplings among them in the DPND6 hexamer. The orange, green and blue double-arrows present the excitonic couplings, hole and electron transfer integrals, respectively. Blue and green isosurfaces with an isovalue of 0.002 a.u. for the quasi-diabatic states correspond to the electron and hole wavefunction distributions. The diabatic energies are given right below the isosurfaces of the different quasi-diabatic states and the coupling values less than 10 meV are omitted.

In Fig. 4 and Fig. 5, the blue and green isosurfaces correspond to electron and hole population distributions in the molecular fragments, respectively. Obviously, the LE, CT and CS states are found in the constructed quasi-diabatic states with regard to the charge and excitation distributions. For the DPND6 aggregate, as shown in Fig. 4, the excitonic couplings (V_{ex}) of the nearest neighbor for energy transfer are about 59 meV, and the second-nearest-neighboring couplings are about 10

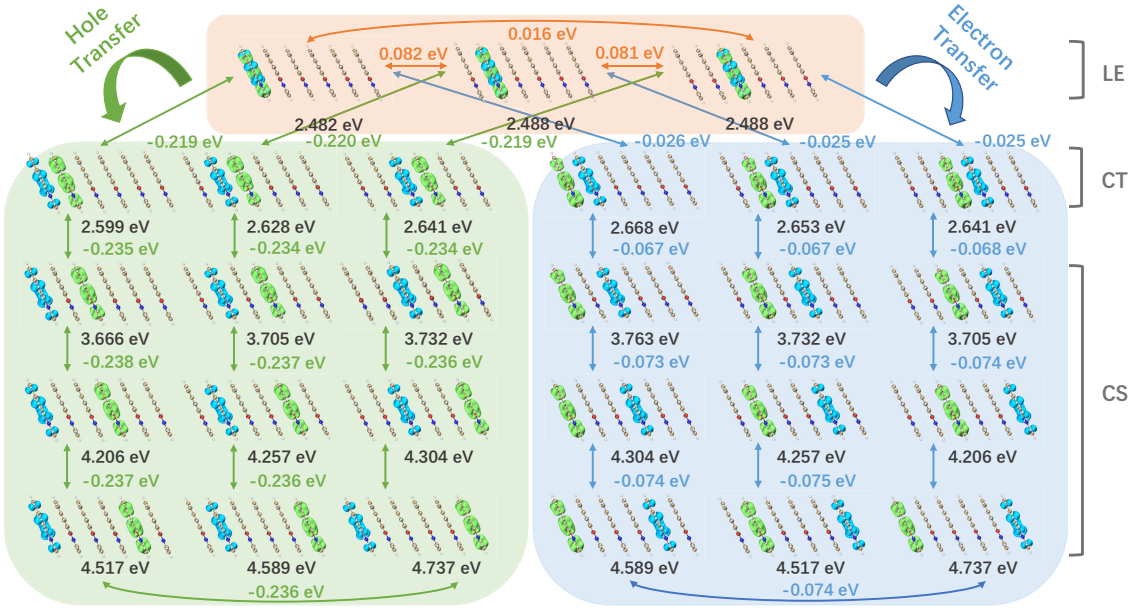

Figure 5: The energies of quasi-diabatic LE, CT and CS states and electronic couplings among them in the DPND hexamer. The orange, green and blue double-arrows present the excitonic couplings, hole and electron transfer integrals, respectively. Blue and green isosurfaces with an isovalue of 0.002 a.u. for the quasi-diabatic states correspond to the electron and hole wavefunction distributions. The diabatic energies are given right below the isosurfaces of the different quasi-diabatic states and the coupling values less than 10 meV are omitted.

meV which cannot be ignored. The exciton dissociation from the LE state to the CT state has two channels, according to electron or hole transfer to the neighbor monomer. The exciton dissociation couplings in terms of the hole transfer (t_h) are about 38 meV, obviously larger than those in terms of electron transfer (t_e). Interestingly, the hole transfer couplings from the CT state to the CS state are about 50 meV, only slightly larger than those from the LE state to the CT state. From the quasi-diabatic energy alignments, it is found that the CT-state energies (E_{CT}) from the hole transfer are slightly (0.15 eV) higher than those of LE states. Moreover, we can obtain that all CS-state energies are 1.0 eV higher than LE-state energies (E_{LE}). The above data manifest that the DPND6 aggregate has a H-type aggregation property and long-range excitation energy transfer cannot be ignored. The exciton dissociation easily occurs via the hole transfer, thus DPND6 should be a good donor candidate because the hole transfer coupling is obviously larger than electron transfer integral. However, the CS-state energies are too high compared with LE-state energies, and the

free electron and hole are thus hardly generated from LE states.

As for the excited-state property of the DPND aggregate shown in Fig. 5, the relative values of all couplings have similar behaviors to those in DPND6, however, the absolute magnitudes of couplings are about two to six times larger than in DPND6 because of a larger overlap between two monomers. These significant differences of electronic coupling strengths may result in the remarkably different mixed characteristics of LE and CT states and different spectral characteristics.

Pure Electronic Absorption Spectra of DPND6 and DPND Aggregates

Based on Kasha's rule, the electronic absorption spectra of molecular dimer should be obviously different from that of monomer due to the couplings between two monomers. It is thus favorable to directly calculate the excitation energies and the oscillator strengths (or pure electronic absorption spectra) of dimer to qualitatively understand the intermolecular interaction from the aggregation effects. Fig. 6 displays the calculated results with a Gaussian broadening in the low-energy regime and the pure electronic absorption spectra of the corresponding monomers are shown for comparison. The DPND6 dimer exhibits two absorption peaks with quite different absorption strength, which are located at 2.45 eV and 2.59 eV and are blue-shifted compared with that of DPND6 monomer (at 2.41 eV). The DPND dimer also exhibits two absorption peaks with nearly identical strength, which are located at 2.34 eV and 2.83 eV, and appear on both sides of the monomer's peak (at 2.48 eV). These spectral properties of dimers cannot be straightforwardly explained by the traditional Kasha model,[45–47] which states that the absorption peak of dimer should be blue- (red-) shifted for H-type (J-type) aggregates compared with the absorption peak of monomer, thus the more complex intermolecular interactions should be taken into account.

To explain the origin of characteristic absorption peaks of two dimers, we analytically study the contributions of the LE and CT states to the low-energy adiabatic electronic excited states of the dimers. Consider a dimer AB, and assume that its two intramolecular LE states (A^*B and AB^*) and two intermolecular CT states (A^+B^- and A^-B^+) determine the low-energy absorption of AB.

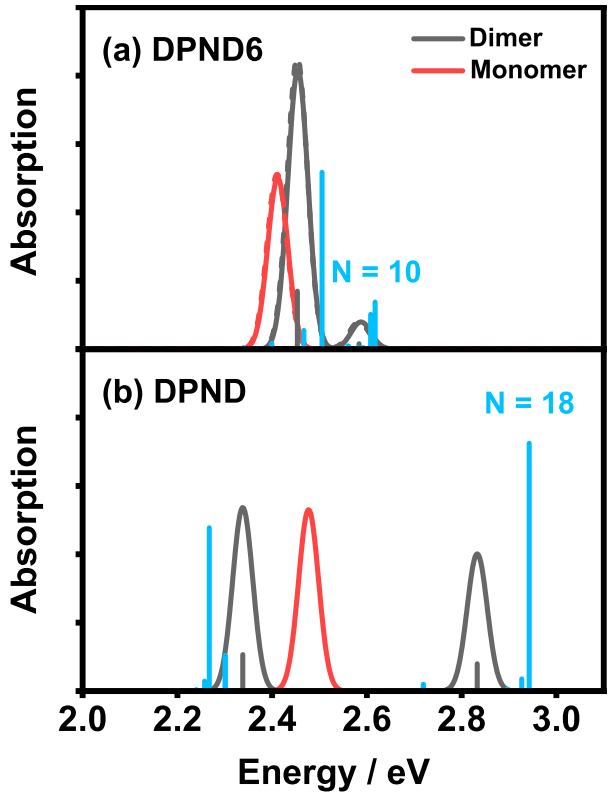

Figure 6: Electronic absorption spectra of (a) DPND6 and (b) DPND dimer. The monomer spectra (red solid line) are presented for comparison. The solid and dash lines in (a) correspond to the DPND with hexyl side chain and ethyl side chain, respectively. The calculated spectra of monomer and dimer are broadened using the Gaussian line shape function with a full width of 0.05 eV. The gray and blue vertical lines in (a) and (b) correspond to the oscillator strengths of dimer and 10-monomer aggregate for DPND6, and dimer and 18-monomer aggregate for DPND, respectively.

For the sake of simplification, we further assume that the A and B molecules are identical, the AB's two LE states have the same energy of E_{LE}, and its two CT states also have same energy of E_{CT}. The mixing of two LE states will produce two new mixing (or FE) states, $\frac{A^*B \pm AB^*}{2}$ with the energy $E_{LE} \pm V_{ex}$, here V_{ex} denotes the excitonic coupling between two LE states. For a H-type dimer, the first FE state with the plus sign is a bright state and the other is a dark state. The mixing of two CT states will also produce two mixing CT states, $\frac{A^+B^- \pm A^-B^+}{2}$, which are dark states and have the energy of E_{CT} since the coupling of two CT states is neglectable small. The further mixing between two FE states and two mixing CT states will only produce two bright FE-CT states, $C_{11}\frac{A^*B+AB^*}{2} + C_{12}\frac{A^+B^- + A^-B^+}{2}$ and $C_{21}\frac{A^*B+AB^*}{2} - C_{22}\frac{A^+B^- + A^-B^+}{2}$ if the symmetries of these

FE and CT states are taken into account. Here C_{ij} is the mixing coefficient, and $|C_{ij}|$ determines the contribution of the $j-$th state (the FE or CT state) to the $i-$th FE-CT state. The larger the value of $|C_{i1}|$, the larger contribution of $\frac{A^*B+AB^*}{2}$ to the dimer's excited state. Subsequently, this adiabatic electronic excited state of the dimer possesses larger oscillator strength than the other. The coupling between $\frac{A^*B+AB^*}{2}$ and $\frac{A^+B^-+A^-B^+}{2}$ is t_e+t_h. In the end, we find that two bright FE-CT states separately possess the energy of $E_\pm = (E_{LE}+E_{CT}+V_{ex}\pm\Delta E)/2$, where $\Delta E = \sqrt{(E_{LE}+V_{ex}-E_{CT})^2+4(t_e+t_h)^2}$.

Now we take the DPND dimer as an example to calculate the energy of two bright excited states. Its corresponding parameters can be estimated according to the diabatization results of the DPND hexamer, and they are $E_{LE}=2.482$, $E_{CT}=2.599$, $V_{ex}=0.082$, $t_e=-0.026$ and $t_h=-0.219$ eV. Based on these parameters, the calculated energy difference (ΔE) between two bright FE-CT states is 0.491 eV, and their corresponding excitation energies are 2.336 and 2.827 eV, respectively, verified that two absorption peaks of this DPND dimer should be located at two sides of the monomer's peak with the excitation energy of 2.48 eV, which are highly in line with the TDDFT calculated results of the DPND dimer. The above analysis has further confirmed that the two absorption peaks of the DPND dimer are indeed from the mixing of FE and CT states.

To further show the effects of long-range excitation energy transfer and aggregation lengths in the electronic absorption spectra, we also display in Fig. 6 the pure electronic absorption spectra of the DPND6 aggregate with 10 monomers and the DPND aggregate with 18 monomers. Here, the electronic-state properties are obtained from the model Hamiltonian constructed from the diabatic results of hexamer. The selected aggregation lengths are long enough to guarantee the electronic states not influenced by the boundary effects. As shown in Fig. 6 (a), two dominate electronic states of the DPND6 aggregate with the great oscillator strengths in two different energy regions are both blue-shifted compared to those of dimer. In the DPND aggregate shown in Fig. 6 (b), the low-energy electronic state is red-shifted whereas the high-energy one is blue-shifted. Moreover, it is quite remarkable that the relative oscillator strengths of low-energy and high-energy electronic states in the DPND aggregate are inverted, compared with the dimer system.

As analyzed in dimers, the different splitting values are closely related to the electronic coupling among electronic coupling states. The relative strengths of peaks may alternatively be explained by the components of mixed states of FE and CT states. In the H-aggregates, the energies of bright FE states will remarkably increase due to the electronic couplings including nearest-neighboring and long-range energy transfer. As the energy of the FE state exceeds that of the CT state, the absorption strength of the high-energy peak from the mixing of FE and CT states may become stronger than that of the low-energy peak. The DPND aggregate indeed shows this behavior, which should be caused by relatively strong nearest-neighboring and long-range excitonic couplings.

This aggregate dependence of absorption energy positions and strengths is important for designing suitable aggregate lengths to control photo-physical processes, such as exciton dissociation and singlet fission. Therefore, we analyze the contributions of CT and LE states

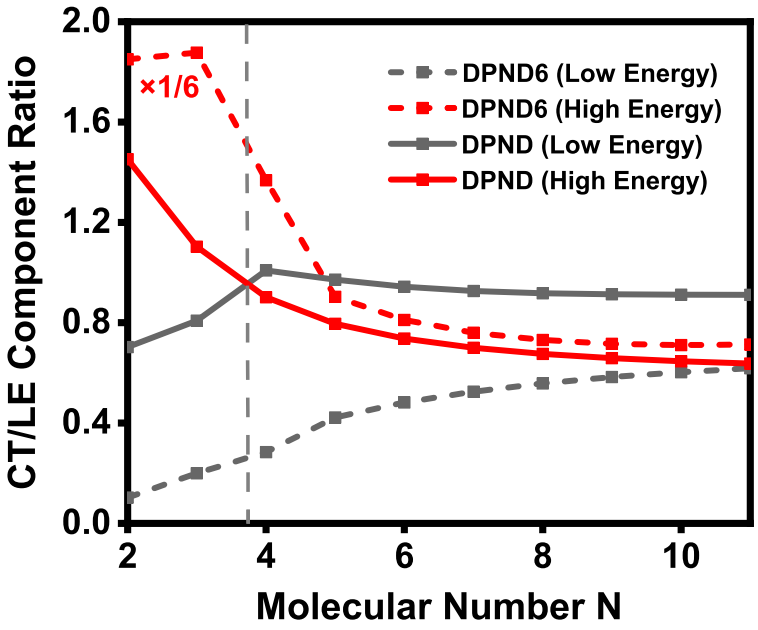

Figure 7: The component ratio of charge transfer states and localized excited states in the low-energy and high-energy absorption peaks in terms of DPND6 and DPND aggregation lengths.

to the states corresponding to two absorption peaks. Fig. 7 displays the ratio of CT/LE components in terms of aggregate lengths. In DPND6 aggregates, the LE-state components in the low-energy

states are always larger than CT-state ones, whereas they are always smaller in the high-energy states. It is expected that absorption strengths of high-energy states cannot exceed those of low-energy states, consistent with spectral calculations. However, in DPND aggregates with more than 4 monomers, the situation completely becomes inverse. In this case, the absorption at the high-energy state becomes stronger than that at the low-energy state. Since the more CT-state components appear in the low-energy states in DPND aggregates, the CT states may be easily generated by photo excitation to benefit charge separation and singlet fission.[48,49]

So far, we have only figured out the pure electronic-state properties of aggregates. To compare with experimental observations, one has to consider the vibrational effect, which may significantly justify the absorption spectra and dynamic processes. In subsequent section, we focus on the vibrationally resolved absorption spectra of aggregates.

Vibrationally Resolved Absorption Spectra of DPND6 and DPND Aggregates

Based on above electronic-state absorption spectra, we calculate the vibrationally resolved absorption spectra of aggregates including 6 to 10 monomers in DPND6 and 6 to 18 monomers in DPND for the purpose of comparison. The calculated spectra as well as experimental observations are shown in Fig. 8, in which the calculated spectra for DPND6 and DPND aggregates are red-shifted by 0.016 eV and blue-shifted by 0.12 eV, respectively. It is noted that the high energy region of the spectra is not included in the present calculations since we only account for few lowest-energy intramolecular LE states and CT states, furthermore the experimental spectra of DPND6 aggregate in high energy region is lack.

The spectra shown in Fig. 8 have two obvious features. Firstly, the spectra for both DPND and DPND6 aggregates are slightly different from one another for the aggregates with more than 6 monomers, manifesting that excitonic coherence lengths in these aggregates should not excess 6 monomers during the excitation dynamic processes. Herein, we only consider the dynamic disorder effect from electron-phonon interactions but ignore the static disorder effect. It can be expected that the incorporation of static disorder should further shorten the coherence lengths.

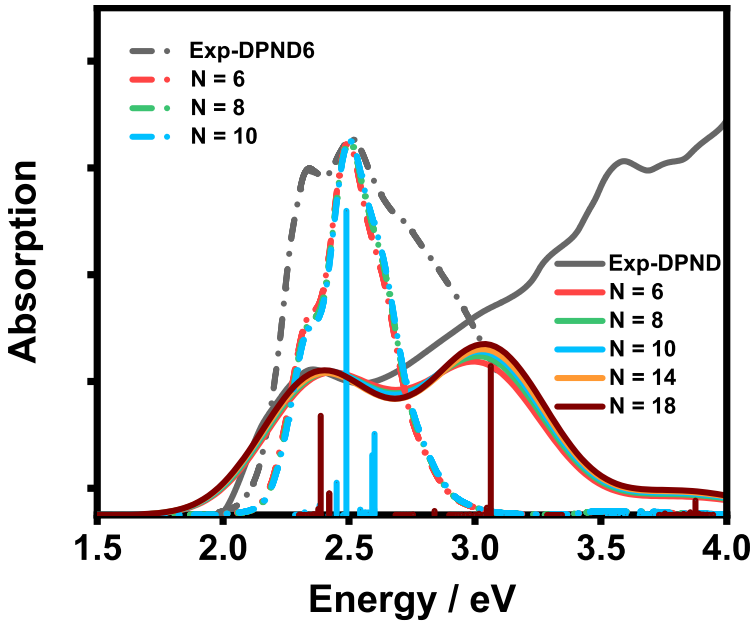

Figure 8: The vibrationally resolved absorption spectra of DPND6 and DPND aggregates at several different aggregation lengths. The damping factors are 0.06 eV and 0.46 eV for DPND6 and DPND aggregates, respectively. The blue and brown vertical lines correspond to the oscillator strengths for the corresponding electronic states in 10-molecule DPND6 aggregates and 18-molecule DPND aggregates.

Secondly, although the DPND aggregates have two obvious peaks and the DPND6 aggregates show one dominant peak with several side peaks, roughly consistent with experimental observations,[12,14] the peak widths are significantly narrower than experimental values, especially in DPND6. It is not clear for this gap between theoretical calculations and experimental observation, and it may be expected that the broadening of experimental spectra may come from the static disorder in aggregates, which is not included in the present calculations. The detailed analysis demonstrates that two absorption peaks of DPND aggregates around 2.4 and 3.0 eV should mainly come from the interaction between the FE and CT states according to the energy values of these electronic states, similar to the dimer case, and the vibrational peaks are immersed by spectral line broadening. It should be addressed that relative strengths of two peaks are inverted caused by excitonic couplings, relative to the dimer.

However, the explanation of DPND6 spectra is not straightforward. To distinguish the contribution of electronic state or vibrational motions to the absorption peaks, we display the pure

electronic-state oscillator strengths with vertical lines for a 10-monomer DPND6 aggregate and a 18-monomer DPND aggregate in Fig. 8. Obviously, two peaks in DPND aggregates indeed mainly correspond to pure electronic excitation, further confirming our above analysis. In the spectra of DPND6, the absorption peaks at 2.50 eV and 2.64 eV mainly correspond to the mixing between the FE and CT states. However, the peak at 2.36 eV corresponds to the vibrational state of the dark electronic state in DPND6 aggregates due to phonon-induced symmetry breaking.[21] Concretely speaking, the first excited state is the dark state in the pure electronic spectra because of H aggregate. As the vibrational motions are incorporated, the oscillator strength from the ground state to the first excited state is not zero due to Franck-Condon factors which break the symmetry of the H-aggregate itself.

Exciton Dynamics in DPND6 and DPND Aggregates

Although the absorption spectra can be used to obtain many significant information on the intramolecular structures and intermolecular interactions, and exhibit the initial populations of LE and CT states after photoexcitation, they cannot obviously reveal the complicated dynamics processes involving exciton dissociation, charge transfer and charge separation with time evolution. Here, we adopt the aggregates composed of 11 monomers to simulate the dynamic processes, and try to investigate the underlying mechanism of remarkably different photo-induced processes in DPND6 and DPND thin films already shown by the experiments.[12,14]

In the dynamic evolution, we firstly choose the photoinduced adiabatic excited states with large oscillator strengths as the initial states which are more likely to be generated after photoexcitation. Fig. 9 displays the excitation energies and corresponding oscillator strengths of adiabatic excited states for two aggregates. Here we obtain the energy levels by diagonalising the effective model Hamiltonian which is composed of the energies of various diabatic states and their couplings. We choose two initial states located in low and high energy regimes with the largest oscillator strengths to simulate the dynamics processes for 11-monomer DPND6 and DPND. For DPND6, these two states correspond to the 11-th (2.506 eV) and 31-th (2.617 eV) electronic states, and for DPND,

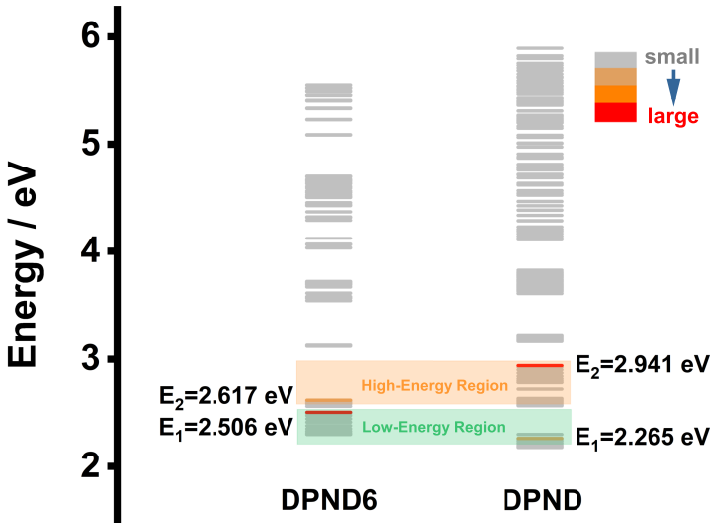

Figure 9: The adiabatic energy-level diagrams of DPND6 and DPND aggregates composed of 11 monomers, calculated from the model Hamiltonian. The colors of energy levels represent the magnitudes of oscillator strengths. E_1 and E_2 are the adiabatic excited states with the largest oscillator strengths in the low-energy and high-energy regions.

they are the 9-th (2.265 eV), 31-th (2.941 eV) electronic states. In the dynamic simulations, we transform these adiabatic states to the diabatic states.

Fig. 10 displays the electronic-state population evolution started from the different initial excited states. It is noted that the effect of the vibrational motions on the population evolution is taken into account via the electron-phonon interactions. The population at $t = 0.0$ illustrates that the initial states of DPND6 and DPND aggregates all contain the components of LE and CT states, verifying the above analysis on spectral characteristics that the main absorption peaks come from the strong mixing between LE and CT states. The relative intensities of the absorption peaks are determined by the proportion of LE states because the CT states are 'dark' states.

Fig. 10 shows that the population exchanges between LE and CT states take place over time. In DPND6 aggregates, the populations of CT states come out a down-up-down-up-down variation both in the low-energy and high-energy region (see Fig. 10 (a) and (c)). However, the time scales of reversed populations of LE and CT states are remarkably different under the influence of initial populations. In DPND aggregates, the population exchanges between LE and CT states happen much faster than in DPND6 due to the strong intermolecular interaction. Otherwise, it can be

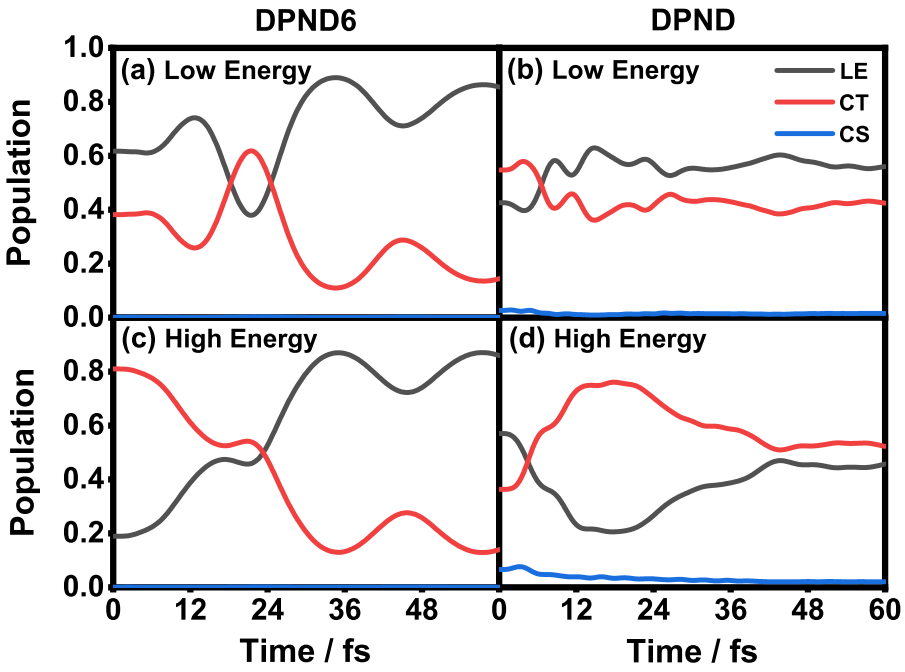

Figure 10: Population evolution of the LE, CT and CS states started from the adiabatic excited states with the excitation energies of (a) 2.506 eV, (c) 2.617 eV and (b) 2.265 eV, (d) 2.941 eV for the DPND6 and DPND aggregates, respectively.

found from Fig. 10 (b) and (d) that the populations of LE and CT states are inverted at the first 5 femtoseconds (fs). The remarkably different dynamic behaviors come from the different stacking arrangements in DPND6 and DPND aggregates. Fig. 3 displays that the relative transverse and longitudinal shift are 3.02 and 1.32 Å in DPND6, whereas they become 0.85 and 1.59 Å in DPND. Those different arrangements cause different electronic couplings. From Fig. 4 and Fig. 5, the excitonic coupling and hole transfer integral between the nearest-neighboring molecules are 0.059 eV and -0.038 eV in DPND6, whereas the relative parameters become 0.081 eV and -0.220 eV in DPND. The much greater hole transfer integral in DPND is more beneficial for the population exchange between LE and CT states than in DPND6 after photoexcitation. The above dynamic results have also demonstrated that the strong intermolecular interactions can promote the population exchange between LE and CT states based on the different population evolution of DPND6 and DPND aggregates. It is also found that DPND6 and DPND aggregates are both hard to generate the charge-separated states directly due to the lack of enough driving forces after

photoexcitation.

Conclusions

By combining the first-principles calculations for constructing the model Hamiltonian and the Non-Markovian stochastic Schrödinger equation for photo-physical simulations, we have theoretically investigated the effect of alkyl side chains on the spectral characteristics and exciton dynamics of the aggregates of DPND skeleton. The results elucidate that the substituent has minor effects on the electronic properties of single molecule, but the existing of alkyl side chains will modulate the intermolecular packing arrangement and affect the intermolecular interactions, subsequently alter the spectral characteristics and exciton dynamics processes.

It has been found that the two main absorption peaks in DPND6 and DPND aggregates at the energy lower 3.5 eV are attributed from the interplay between the FE and CT states. The remarkable differences in spectral shapes of the two aggregates come from the different energy gaps and couplings among LE and CT states, causing the different degree of mixing of LE and CT states. In DPND6, this two states only have an energy spacing of ~ 0.1 eV and the low-energy state predominates the optical absorption. While the two states in DPND have an energy spacing of ~ 0.6 eV and the high-energy absorption strength can even exceed the low-energy one for the aggregates with more than 4 monomers. The vibrational progressions in the absorption spectra of two aggregates are not obvious, however, the lowest-energy absorption peak of DPND6 comes from the transition between the electronic ground state and the vibrational levels of electronic dark excited state. The exciton dynamics simulations demonstrate that the time scales of population exchange between LE and CT states are much faster in DPND aggregates than in DPND6 aggregates due to the stronger intermolecular interaction, which makes the DPND favorable for the use of CT state properties. However, it is difficult for the photoexcitation to directly generate the charge-separated states in both aggregates due to the lack of enough driving forces.

Supporting Information Available

Supplementary data include the energies and transition dipole moments of quasi-diabatic states; electronic couplings between the quasi-diabatic states of the DPND6 and DPND hexamer; electron-phonon coupling constants of all vibrational modes associated with the different electronic states including the localized excited, cationic and anionic states of the DPND6 and DPND single molecule in the crystal environment.

Acknowledgement

This work is supported by the National Science Foundation of China (Grant Nos. 21833006, 22173074 and 22033006).

References

(1) Eng, J.; Penfold, T. J. Open Questions on the Photophysics of Thermally Activated Delayed Fluorescence. *Commun. Chem.* **2021**, *4*, 1–4.

(2) Theurer, C. P.; Valencia, A. M.; Hausch, J.; Zeiser, C.; Sivanesan, V.; Cocchi, C.; Tegeder, P.; Broch, K. Photophysics of Charge Transfer Complexes Formed by Tetracene and Strong Acceptors. *J. Phys. Chem. C* **2021**, *125*, 6313–6323.

(3) Park, S. Y.; Chandrabose, S.; Price, M. B.; Ryu, H. S.; Lee, T. H.; Shin, Y. S.; Wu, Z.; Lee, W.; Chen, K.; Dai, S. et al. Photophysical Pathways in Efficient Bilayer Organic Solar Cells: The Importance of Interlayer Energy Transfer. *Nano Energy* **2021**, *84*, 105924.

(4) Mohapatra, A. A.; Tiwari, V.; Patil, S. Energy Transfer in Ternary Blend Organic Solar Cells: Recent Insights and Future Directions. *Energy Environ. Sci.* **2021**, *14*, 302–319.

(5) Song, W.; Zhi, J.; Wang, T.; Li, B.; Ni, S.; Ye, Y.; Wang, J.-L. Tetrathienylethene-based Positional Isomers with Aggregation-induced Emission Enabling Super Red-shifted Reversible Mechanochromism and Naked-eye Sensing of Hydrazine Vapor. *Chem. Asian J.* **2019**, *14*, 3875–3882.

(6) Qiu, Z.; Yang, Z.; Chen, W.-C.; Xing, L.; Hu, S.; Ji, S.; Yang, Q.; Cai, N.; Ouyang, X.; Huo, Y. Alkoxy Chain Regulated Stimuli-Responsive AIE Luminogens Based on Tetraphenylethylene Substituted Phenanthroimidazoles and Non-Doped OLEDs with Negligible Efficiency Roll-Off. *J. Mater. Chem. C* **2020**, *8*, 4139–4147.

(7) Kang, L.; Chao, A.; Zhang, M.; Yu, T.; Wang, J.; Wang, Q.; Yu, H.; Jiang, N.; Zhang, D. Modulating the Molecular Geometry and Solution Self-Assembly of Amphiphilic Polypeptoid Block Copolymers by Side Chain Branching Pattern. *J. Am. Chem. Soc.* **2021**, *143*, 5890–5902.

(8) Liu, K.-K.; Huang, H.; Wang, J.-L.; Wan, S.-S.; Zhou, X.; Bai, H.-R.; Ma, W.; Zhang, Z.-G.; Li, Y. Modulating Crystal Packing, Film Morphology, and Photovoltaic Performance of Selenophene-Containing Acceptors through a Combination of Skeleton Isomeric and Regioisomeric Strategies. *ACS Appl. Mater. Interfaces* **2021**, *13*, 50163–50175.

(9) Jiang, Y.-Y.; Liu, H.; Li, T.; Zhang, K.; Gao, P.-F.; Zhou, M.-S.; Zhang, L.-L.; Fu, H.-R. Coordination-Induced Approach of a Carbazole-Based Molecule to Modulate Packing Modes for Ultralong Room-Temperature Phosphorescence. *Cryst. Growth Des.* **2022**, *22*, 2725–2732.

(10) Hu, S.; Yao, Z.; Ma, X.; Yue, L.; Chen, L.; Liu, R.; Wang, P.; Li, H.; Zhang, S.-T.; Yao, D. et al. Pressure-Induced Local Excitation Promotion: New Route toward High-Efficiency Aggregate Emission Based on Multimer Excited State Modulation. *J. Phys. Chem. Lett.* **2022**, *13*, 1290–1299.

(11) Grzybowski, M.; Deperasińska, I.; Chotkowski, M.; Banasiewicz, M.; Makarewicz, A.; Kozankiewicz, B.; Gryko, D. T. Dipyrrolonaphthyridinediones–Structurally Unique Cross-Conjugated Dyes. *Chem. Comm.* **2016**, *52*, 5108–5111.

(12) Wang, L.; Lin, L.; Yang, J.; Wu, Y.; Wang, H.; Zhu, J.; Yao, J.; Fu, H. Singlet Fission in a Pyrrole-Fused Cross-Conjugated Skeleton with Adaptive Aromaticity. *J. Am. Chem. Soc.* **2020**, *142*, 10235–10239.

(13) Sadowski, B.; Kaliszewska, M.; Poronik, Y. M.; Czichy, M.; Janasik, P.; Banasiewicz, M.; Mierzwa, D.; Gadomski, W.; Lohrey, T. D.; Clark, J. A. et al. Potent Strategy towards Strongly Emissive Nitroaromatics through a Weakly Electron-Deficient Core. *Chem. Sci.* **2021**, *12*, 14039–14049.

(14) Wang, L.; Cai, W.; Sun, J.; Wu, Y.; Zhang, B.; Tian, X.; Guo, S.; Liang, W.; Fu, H.; Yao, J. H-Type-like Aggregation-Accelerated Singlet Fission Process in Dipyrrolonaphthyridinedione

Thin Film: The Role of Charge Transfer/Excimer Mixed Intermediate State. *J. Phys. Chem. Lett.* **2021**, *12*, 12276–12282.

(15) Monahan, N.; Zhu, X.-Y. Charge Transfer–Mediated Singlet Fission. *Annu. Rev. Phys. Chem.* **2015**, *66*, 601–618.

(16) Miller, C. E.; Wasielewski, M. R.; Schatz, G. C. Modeling Singlet Fission in Rylene and Diketopyrrolopyrrole Derivatives: The Role of the Charge Transfer State in Superexchange and Excimer Formation. *J. Phys. Chem. C* **2017**, *121*, 10345–10350.

(17) Felter, K. M.; Grozema, F. C. Singlet Fission in Crystalline Organic Materials: Recent Insights and Future Directions. *J. Phys. Chem. Lett.* **2019**, *10*, 7208–7214.

(18) Sher, P.-H.; Chen, C.-H.; Chiu, T.-L.; Lin, C.-F.; Wang, J.-K.; Lee, J.-H. Distinct Routes of Singlet Fission and Triplet Fusion: A Fluorescence Kinetic Study of Rubrene. *J. Phys. Chem. C* **2019**, *123*, 3279–3284.

(19) Mayonado, G.; Vogt, K. T.; Van Schenck, J. D. B.; Zhu, L.; Fregoso, G.; Anthony, J.; Ostroverkhova, O.; Graham, M. W. High-Symmetry Anthradithiophene Molecular Packing Motifs Promote Thermally Activated Singlet Fission. *J. Phys. Chem. C* **2022**, *126*, 4433–4445.

(20) Hestand, N. J.; Spano, F. C. Expanded Theory of H- and J-Molecular Aggregates: The Effects of Vibronic Coupling and Intermolecular Charge Transfer. *Chem. Rev.* **2018**, *118*, 7069–7163.

(21) Feng, S.; Wang, Y.-C.; Ke, Y.; Liang, W.; Zhao, Y. Effect of Charge-Transfer States on the Vibrationally Resolved Absorption Spectra and Exciton Dynamics in ZnPc Aggregates: Simulations from a Non-Makovian Stochastic Schrödinger Equation. *J. Chem. Phys.* **2020**, *153*, 034116.

(22) Feng, S.; Wang, Y.-C.; Liang, W.; Zhao, Y. Vibrationally Resolved Absorption Spectra and

Exciton Dynamics in Zinc Phthalocyanine Aggregates: Effects of Aggregation Lengths and Remote Exciton Transfer. *J. Phys. Chem. A* **2021**, *125*, 2932–2943.

(23) Feng, S.; Wang, Y.-C.; Liang, W.; Zhao, Y. Vibrationally Resolved Absorption Spectra and Ultrafast Exciton Dynamics in α-Phase and β-Phase Zinc Phthalocyanine Aggregates. *Phys. Chem. Chem. Phys.* **2022**, *24*, 2974–2987.

(24) Swathi, R. S.; Sebastian, K. L. Long Range Resonance Energy Transfer from a Dye Molecule to Graphene Has (Distance)$^{-4}$ Dependence. *J. Chem. Phys.* **2009**, *130*, 086101.

(25) Natali, M.; Campagna, S.; Scandola, F. Photoinduced Electron Transfer across Molecular Bridges: Electron- and Hole-Transfer Superexchange Pathways. *Chem. Soc. Rev.* **2014**, *43*, 4005–4018.

(26) Liu, X.; Liu, J. Path Integral Molecular Dynamics for Exact Quantum Statistics of Multi-Electronic-State Systems. *J. Chem. Phys.* **2018**, *148*, 102319.

(27) Liu, Z.; Lu, T.; Chen, Q. Vibrational Spectra and Molecular Vibrational Behaviors of All-Carboatomic Rings, Cyclo[18]Carbon and Its Analogues. *Chem. Asian J.* **2021**, *16*, 56–63.

(28) Yan, Y.; Liu, Y.; Xing, T.; Shi, Q. Theoretical Study of Excitation Energy Transfer and Nonlinear Spectroscopy of Photosynthetic Light-Harvesting Complexes Using the Nonperturbative Reduced Dynamics Method. *WIREs Comput Mol Sci.* **2021**, *11*, e1498.

(29) Wang, Y.-C.; Feng, S.; Liang, W.; Zhao, Y. Electronic Couplings for Photoinduced Charge Transfer and Excitation Energy Transfer Based on Fragment Particle–Hole Densities. *J. Phys. Chem. Lett.* **2021**, *12*, 1032–1039.

(30) Wang, Y.-C.; Ke, Y.; Zhao, Y. The Hierarchical and Perturbative Forms of Stochastic Schrödinger Equations and Their Applications to Carrier Dynamics in Organic Materials. *WIREs Comput Mol Sci.* **2019**, *9*, e1375.

(31) Ness, H.; Shevlin, S. A.; Fisher, A. J. Coherent Electron-Phonon Coupling and Polaronlike Transport in Molecular Wires. *Phys. Rev. B* **2001**, *63*, 125422.

(32) Giustino, F.; Cohen, M. L.; Louie, S. G. Electron-Phonon Interaction Using Wannier Functions. *Phys. Rev. B* **2007**, *76*, 165108.

(33) Giustino, F. Electron-Phonon Interactions from First Principles. *Rev. Mod. Phys.* **2017**, *89*, 015003.

(34) Santoro, F.; Cappelli, C.; Barone, V. Effective Time-Independent Calculations of Vibrational Resonance Raman Spectra of Isolated and Solvated Molecules Including Duschinsky and Herzberg-Teller Effects. *J. Chem. Theory Comput.* **2011**, *7*, 1824–1839.

(35) Ferrer, F. J. A.; Barone, V.; Cappelli, C.; Santoro, F. Duschinsky, Herzberg-Teller, and Multiple Electronic Resonance Interferential Effects in Resonance Raman Spectra and Excitation Profiles. The Case of Pyrene. *J. Chem. Theory Comput.* **2013**, *9*, 3597–3611.

(36) Ma, H. L.; Zhao, Y.; Liang, W. Z. Assessment of Mode-Mixing and Herzberg-Teller Effects on Two-Photon Absorption and Resonance Hyper-Raman Spectra from a Time-Dependent Approach. *J. Chem. Phys.* **2014**, *140*, 94107.

(37) Nuraliev, M. K.; Parashchuk, O. D.; Tukachev, N. V.; Repeev, Y. A.; Maslennikov, D. R.; Borshchev, O. V.; Vainer, Y. G.; Paraschuk, D. Y.; Sosorev, A. Y. Toward Probing of the Local Electron–Phonon Interaction in Small-Molecule Organic Semiconductors with Raman Spectroscopy. *J. Chem. Phys.* **2020**, *153*, 174303.

(38) Zhong, X.; Zhao, Y. Non-Markovian Stochastic Schrödinger Equation at Finite Temperatures for Charge Carrier Dynamics in Organic Crystals. *J. Chem. Phys.* **2013**, *138*, 014111.

(39) Ke, Y.; Zhao, Y. Perturbation Expansions of Stochastic Wavefunctions for Open Quantum Systems. *J. Chem. Phys.* **2017**, *147*, 184103.

(40) Johnson, R. D. NIST Computational Chemistry Comparison and Benchmark Database. http://cccbdb.nist. gov/ (accessed May 22, 2022).

(41) Frisch, M. J.; Trucks, G. W.; Schlegel, H. B.; Scuseria, G. E.; Robb, M. A.; Cheeseman, J. R.; Scalmani, G.; Barone, V.; Petersson, G. A.; Nakatsuji, H. et al. *Gaussian 16*, Revision A.03; Gaussian, Inc.: Wallingford, CT, 2016.

(42) Marenich, A. V.; Cramer, C. J.; Truhlar, D. G. Universal Solvation Model Based on Solute Electron Density and on a Continuum Model of the Solvent Defined by the Bulk Dielectric Constant and Atomic Surface Tensions. *J. Phys. Chem. B* **2009**, *113*, 6378–6396.

(43) Lu, T.; Chen, F. Multiwfn: A Multifunctional Wavefunction Analyzer. *J. Comput. Chem.* **2012**, *33*, 580–592.

(44) Humphrey, W.; Dalke, A.; Schulten, K. VMD: Visual Molecular Dynamics. *J. Mol. Graph.* **1996**, *14*, 33–38.

(45) Kasha, M. Characterization of Electronic Transitions in Complex Molecules. *Discuss. Faraday Soc.* **1950**, *9*, 14.

(46) McRae, E. G.; Kasha, M. Enhancement of Phosphorescence Ability upon Aggregation of Dye Molecules. *J. Chem. Phys.* **1958**, *28*, 721–722.

(47) Kasha, M. Relation between Exciton Bands and Conduction Bands in Molecular Lamellar Systems. *Rev. Mod. Phys.* **1959**, *31*, 162–169.

(48) Zang, H.; Zhao, Y.; Liang, W. Quantum Interference in Singlet Fission: J-and H-Aggregate Behavior. *J. Phys. Chem. Lett.* **2017**, *8*, 5105–5112.

(49) Johnson, J. C. Open Questions on the Photophysics of Ultrafast Singlet Fission. *Commun. Chem.* **2021**, *4*, 1–3.